STRUCTURAL AND OPTICAL PROPERTIES OF SOL-GEL SYNTHESIZED TiO$_2$ NANOCRYSTALS: EFFECT OF Ni AND Cr (CO)DOPING

Olim Ruzimuradov [a,b,c *], Khusniddin Musaev [b], Shavkat Mamatkulov [c], Khakimjan Butanov [c,d], Isabel Gonzalo-Juan [e], Liudmila Khoroshko [f,g], Nurmuhammad Turapov [b], Suvonkul Nurmanov [b], Jamoliddin Razzokov [h,i], Victor Borisenko [f], Ralf Riedel [e]

[a] *Department of Natural and Mathematic Sciences, Turin Polytechnic University in Tashkent, Kichik Halqa Yo'li 17, Tashkent 100095, Uzbekistan*
[b] *Department of Chemistry, National University of Uzbekistan, Vuzgorodok 15, Tashkent 100174, Uzbekistan*
[c] *Institute of Material Sciences of the Academy of Sciences of the Republic of Uzbekistan, Chingiz Aytmatov 2b, Tashkent 100084, Uzbekistan*
[d] *National Scientific Research Institute of Renewable Energy Sources under Ministry of Energy of the Republic of Uzbekistan, Chingiz Aytmatov 2b, Tashkent 100084, Uzbekistan*
[e] *Technische Universität Darmstadt, Institut für Materialwissenschaft, Otto-Berndt-Straße 3, D-64287 Darmstadt, Germany*
[f] *Belarusian State University of Informatics and Radioelectronics, P. Browka 6, Minsk, 220013, Belarus*
[g] *Belarusian State University, Faculty of Physics, 4 Nezavisimosti Av., 220030 Minsk, Belarus*
[h] *Institute of Fundamental and Applied Research, National Research University TIIAME, Kori Niyoziy 39, 100000, Tashkent, Uzbekistan*
[i] *College of Engineering, Akfa University, Milliy Bog Street 264, 111221, Tashkent Uzbekistan*

---

*Corresponding author: o.ruzimuradov@polito.uz (OR)

Abstract:

Nickel and chromium metal ions have been utilized to dope and co-dope titanium dioxide nanocrystals, thereby broadening the light absorption range of titania into the visible light spectrum. The doped and co-doped TiO2 nanocrystals were prepared using sol-gel techniques, with a varied doping concentration that extended from 0.25 to 10.0 wt.%. These modified materials underwent comprehensive analysis using standard analytical tools such as X-ray diffraction, Raman spectroscopy, BET surface area measurement, Fourier transform infrared spectroscopy, UV-vis diffuse reflectance spectroscopy, and fluorescence spectroscopy. The Powder XRD method uncovered that the reformed catalyst predominantly comprises the anatase polymorph, with the transition metal ion either taking the place of Ti or situated as interstitials in the TiO2 lattice. When metal ion concentration rose from 0.25 to 10 wt.%, Raman and UV-Vis absorption spectrums of the doped and co-doped catalyst exhibited a λ_{max} shift towards a longer wavelength.

Fourier Transform Infrared (FTIR) spectra revealed the stretching and vibrational behavior of hydroxyl radicals in the nanocrystals. The BET surface area of the doped and co-doped TiO_2 nanocrystals significantly surpassed that of the undoped TiO_2.

Electronic structural studies of the TiO_2, $(Ti,Cr)O_2$, $(Ti,Ni)O_2$, and $(Ti,Ni,Cr)O_2$ crystals using density functional theory indicated a reduction in the band gap width (E_g) of pure TiO_2 when doped with transition metals. Specifically, the indirect bandgap values for Ni(10%), Cr(10%) and NiCr(5%+5%) doping were 2.96, 2.83, and 2.7 eV, respectively. Furthermore, the photoluminescence intensity substantially decreased with the integration of transition metal ions in the TiO_2 nanocrystals.

contain

2

1. Introduction

Numerous strategies have been explored to boost the photocatalytic efficiency of TiO_2. Of these, doping is a potent technique that can effectively reduce the band gap, thereby empowering TiO_2 with the ability to absorb visible light and augment the rate of electron-hole separation [1-3].

In recent years, significant endeavors have been made to alter the electronic structure of TiO_2 materials. One potent tactic involves doping TiO_2 with various cations and anions, a method that serves to decrease its band gap and enhance its absorption of visible light. Strategies to elevate the efficiency of semiconductors encompass the integration of transition metals via doping. This procedure replaces a certain amount of Ti atoms with doped metal ions, thereby injecting new energy levels into the band structure, which effectively assists in trapping electrons or holes and separating carriers from the bands. Consequently, a larger number of carriers can successfully diffuse to the surface, thereby boosting the semiconductor's performance. Certain proposals suggest that the necessary red shift for the absorption edge could be achieved by amplifying the concentration of impurity ions or the oxygen defects in TiO_2 [4, 5]. The intention behind doping is to manipulate the extensive bandgap and electronic structure of a material to enhance its optical properties in the visible light spectrum. Additionally, it aims to optimize every stage of charge kinetics in order to significantly curb the recombination of photogenerated carriers. Doping also seeks to elevate the characteristics of the interface and surface for improved performance. [6]. However, photocatalytic activity is highly dependent on the exposed crystalline interfaces [7, 8]. Metal ions, such as alkaline-earth [9, 10] and transition metals [11-13], have been researched as potential dopants for photocatalytic activities. Specifically, alkaline-earth and transition metals have displayed visible-light photocatalytic activities. To further improve the visible-light photocatalytic activity of TiO2, co-doping with two metal ions has been attempted [14-18]. Research has been conducted on numerous metal ions, but progress has been made on specific ones.

3

Introducing metal ions into the TiO2 lattice results in more than just a reduction in the band gap; it also stimulates several fascinating effects. These encompass enhancing the photocatalytic activity of the TiO2 electrodes by curbing the recombination rate of electrons and holes, alterations in the surface charge carrier trap population, and modifications in the kinetics of electron (e-) and hole (h+) transfer. This approach demonstrates significant potential in boosting the efficacy of TiO2 electrodes [15–18].

Choi et al. [14] explored the impact of co-doping various types of metal ions (Pt, Cr, V, and Ni) on TiO2 using the sol-gel method with doping levels ranging from 0.1 to 0.5 at.%. Additionally, Li et al. developed a new category of visible light-sensitive photocatalysts - W and Mn co-doped and anchored visible-light-absorbing TiO2 films, created via the layer-by-layer technique. Their studies indicated that Mn and W as dopants not only narrow the band gap to encompass the visible region, but also expedite the detrapping of charge carriers to the catalyst surface [15]. Research has also demonstrated that Fe-Mo co-doping of TiO2 enhances the photocatalytic activity for O2 evolution under exposure to visible-light irradiation [16]. In another study, Zhu et al examined the electronic and optical properties of anatase and rutile TiO2 doped with Fe or/and Ni (co)doping, employing the spin-polarized density functional theory [17]. The computed results have revealed that the synergestic impact of (Fe + Ni) co-doping leads to a contraction of the band gap in TiO2 nanomaterials. This also results in the emergence of hybridized states of Fe 3d and Ni 3d within the band gap. Consequently, a significant enhancement occurred in the optical absorption of the nanomaterials extending from the ultraviolet-light to the infrared-light region. This, in turn, brings about a considerable decrease in the recombination of photogenerated electron-hole pairs.

Recently, in a study by Garg et al. [18], it was found that doped and co-doped samples demonstrated a marginal rise in the diffraction angle for the (101) crystalline plane of anatase when compared to pure TiO2, corresponding with an increase in the doping percentage of Fe and Cu ions.

4

This observation suggests that the dopants, coupled with their reduced ionic radii, induce a transformation in the lattice structure of the anatase configuration within the TiO2 matrix.

While most of the earlier studies primarily focused on the outcomes of doping with single metallic and non-metallic ions, more recent research has broadened to include co-doping with two ions. This shift underscores the potential cooperative impacts of the dopants in boosting the photocatalytic performance [19-24]. To our knowledge, there have been few reports examining the physical and chemical processes involved in creating Ni and Cr-doped TiO_2, especially the fundamental reasons driving the distinct optical absorption and redox potential of Ni and Cr metals when co-doping TiO_2 materials. To address these queries, we have carried out an in-depth analysis of the combined effect of (Ni-Cr) doping of TiO_2 on the red shift mechanism in the optical absorption edge and the origin of the improved visible light photocatalytic efficiency, utilizing spin-polarized DFT calculations. Our study delves into the redox potential of Ni or/and Cr (co)doped TiO_2 photocatalysts and helps to better understand the influence of the electronegativity of Ni and Cr when co-doping TiO_2 on its photocatalytic properties. This exploration will offer fresh perspectives in comprehending the physical and chemical mechanisms behind the enhanced visible-light photocatalytic activity of (Ni-Cr)-co-doped TiO_2. Furthermore, it will contribute to the design of advanced photocatalytic materials tailored with the necessary electronic properties.

2. Experimental

2.1. Synthesis

We adopted the sol-gel method for preparation of single or double-doped titania by modification of the procedure reported previously elsewhere [25]. In the single-doped process (M-TiO_2), we sequentially added aqueous solution of HCl (33%), $Ti(O^nPr)_4$, formaldehyde (FA), and H_2O infused with $Ni(NO_3)_2 \cdot x\ 6H_2O$ into a glass vessel. This vessel was cooled with an ice bath and subject

to vigorous stirring to prevent the sudden precipitation of titania gel. The typical initial composition was $Ti(OnPr)_4:HCl:FA:H_2O:Ni(NO_3)_2 \cdot 6H_2O = 1:0.5:0.5:x:0.12$ in molar ratio for the Ni –doped TiO_2 with 10 wt% NiO, where x was ranged between 17 and 21. We also varied the content of $Ni(NO_3)_2 \cdot 6H_2O$ in experiments to investigate the impact ofNi content. The same procedure was implimented with the inclusion of $Cr(NO_3)_3 \cdot x\ 9H_2O$.

Double-doped TiO_2 samples (MM´-TiO_2) were prepared by adding two metal precursor aqueous solutions to the initial mixture to give a doping concentration between 0.25 and 10 wt.%. After stirring the mixed solution for 5 minutes, it was sealed and then maintained at 30 °C for 24 hours, during which gelation occurred. The resultant wet gel was dried at 50 °C for several days and then heated at either 500 or 600 °C for a duration of 2 h. Table 1 provides a summary of the Ni and Cr content of the prepared samples.

Table 1. The Ni and Cr contents of the synthesized doped titania samples and the full width at half maximum (FWHM) of the anatase lattice plane (1 0 1) and the crystallite sizes derived therefrom via the Scherrer equation.

Sample	Ni (wt.%)	Cr (wt.%)	FWHM	Crystallite size (nm)
5Ni	5	-	0.41798	91.38
10Ni	10	-	0.456	84.17
5Cr	-	5		132.35
10Cr	-	10	0.475	80.80
2.5Ni2.5Cr	2.5	2.5	0.3568	107.57
5Ni5Cr	5	5	0.52698	72.83

6

2.2. Characterization

The powder X-ray diffraction (XRD) patterns of the synthesized samples were documented on using a STADI P X-ray diffractometer (STOE&Cie GmbH). This device is equipped with a position-sensitive detector, used Mo Kα ($\lambda = 0.7093$ Å) radiation under condition of 60 kV voltage and 50 mA current, capturing the 2θ range of 5-40°. The specific surface area (SSA) of the samples was determined by measuringthe N_2-gas adsorption- desorption isotherms (Autosorb AS6, QuantaChrome). SSA values were calculated by fitting theinitial seven points (relative pressures of 0.05–0.3) of the adsorption branch of the isotherm to the Brunauer–Emmett–Teller (BET) equation. The Fourier transform infrared (FTIR) spectroscopy measurement was carried out using a VARIAN 670-IR FTIR spectrometer, using the attenuated total reflection (ATR) mode, across a range of 550-4000 cm^{-1}.

The ultraviolet - visible diffuse reflectance (UV-vis DR) spectra were recorded at room temperature, utiling a Perkin Elmer Lambda 900 UV/VIS/NIR Spectrometer. The optical band gap energy of the Ni and Cr (co)doped TiO_2 samples estimated from a Tauc plot of $(\alpha h\nu)^2$ versus photon energy $h\nu$. The absorption coefficient (α) calculated from the UV-Vis absorbance data using the Beer-Lambert law. Photoluminescence evaluations were conducted with a VARIAN Cary Eclipse fluorescence spectrophotometer, using a wavelength of 254 nm.

2.3 Calculation models and methods

All of the ab initio calculations were carried out within the framework of density functional theory (DFT) [26], using the Quantum Espresso software package [27]. The kinetic cutoff energy for plane waves was taken as 400 eV and Monkhorst-Pack k-point $3\times3\times3$ grid were used to optimize the geometry and to calculate the electronic structure. The K-point was chosen relative to the spatial group $I4_1/amd$, which contains the following high symmetry points Γ|X|M||Γ|Z|R|A|Z|X|R|M|A [28].

The Perdew-Burke-Ernzerhof (PBE) function in conjuction of generalized gradient approximation were used to calculate exchange-correlation effects. For our calculations, we utilized a supercell composed of 72 oxygen atoms and 36 titanium atoms. This configuration was achieved by

7

applying a (3x3x1) translation to the anatase unit cell and then substituting one titanium atom with either a chromium or nickel atom. (Figure S1 in supporting info). The lattice parameters were optimized until the values of residual forces became less than 0.01 eV/A. The main pitfall of semiconductor calculations by DFT method is the well-known underestimation of the band gap width. To counterbalance this inaccuracy, we employed the method that introduces one-center Hubbard type corrections to Coulomb and exchange interactions in atoms (GGA+U) [29]. According to reported literature data [30], the values Ti(U,J)=(8.0,0.2), Ni(U,J)=(5.0, 0) and Cr(U,J)=(6.0, 0) eV were used for titanium, chromium and nickel atom, leading to agreement of the calculated bandgap width in pure anatase with the experimental data, 3.20-3.42 eV [31]. For pure TiO_2 performed spin-limited GGA+U calculations, and for compounds $Ti_{36-x}Cr_xO_{72}$, $Ti_{36-x}Ni_xO_{72}$ and $Ti_{36-x}Ni_{x/2}Cr_{x/2}O_{72}$ performed spin-polarized GGA+U calculations taking into account the ferromagnetic ordering of chromium and nickel atoms for titanium dioxide structure with parameters of tetragonal body-centered lattice a=b=3 7845 Å, c=9.5143 Å [32]. The x-value was varied from 3 to 6, which corresponds to nickel and chromium concentrations in titanium dioxide of 5.0% and 10% m.d. The valence electrons included in the calculations for oxygen O- $2s^2$ $2p^4$, titanium Ti- $3d^2$ $4s^2$, Cr- $3d^5$ $4s^1$, and Ni - $3d^8$ $4s^2$.

3. Results and discussion

3.1 Morphology, structure and optical properties

Investigations of the surface morphology and chemical composition of both doped and co-doped TiO2 catalysts were conducted through the use of Field Emission Scanning Electron Microscopy (FESEM) and Energy-Dispersive X-ray (EDX) analyses. The findings from these studies are depicted in Figure 1 and Figure 2..
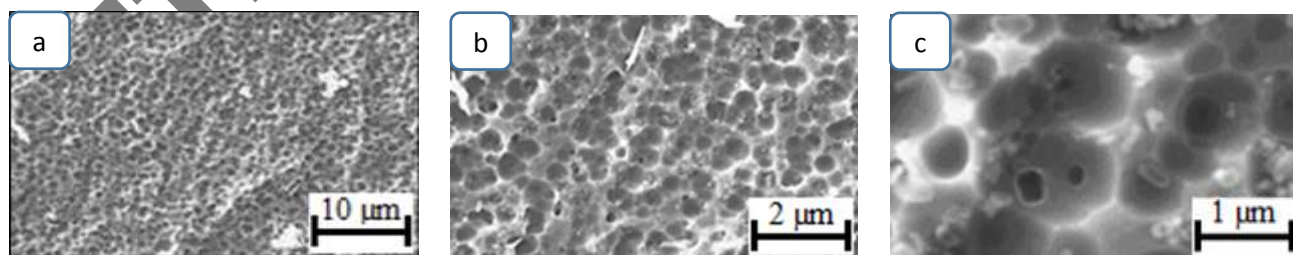

Figure 1. FESEM images of (a, b, c) TiO_2 co-doped with 5wt% of Ni & 5 wt% of Cr.

The Scanning Electron Microscopy (SEM) images of the doped and co-doped TiO$_2$ (Figure 1) presents spherical-shaped particles that have clumped together and display a non-uniformsize distribution. Among these, the Ni-Cr-TiO$_2$ sample illustrated in Figure 1, indicates a substantial reduction in both agglomeration and particle sizes when compared to the doped TiO$_2$. These evidences suggest that the combined doping of Ni and Cr contributes to a significant decline in both agglomeration and particle size in TiO$_2$. Additionally, Energy-Dispersive X-ray (EDX) spectrum of the co-doped TiO$_2$ (Figure 2) reveals the peaks corresponding to Ni and Cr, which are absent in the undoped TiO$_2$ (Figure 2a).
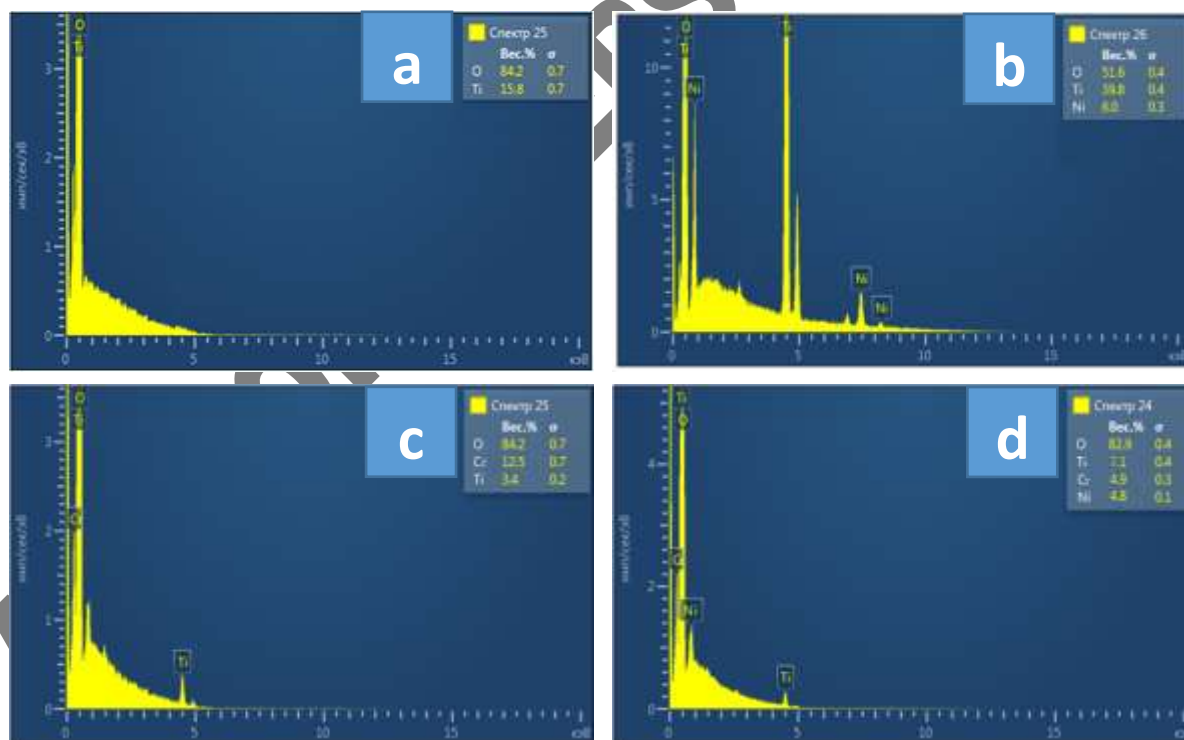

Figure 2. EDX spectrum of (a) undoped TiO$_2$, (b) 5 wt% of Ni doped TiO$_2$, (c) 5 wt% of Ni doped TiO$_2$, (d) 5wt% of Ni & 5 wt% of Cr co-doped TiO$_2$.

Typical X-ray diffraction (XRD) patterns of the as-synthesized Ni and Cr single doped and co-doped TiO$_2$ nanocrystals (NCs) are shown in Figure 3. The samples exhibit diffraction peaks at around $2\theta = 11.5$, 17.0, 22.0, 24.0, 24.8, and 28.0° which are assigned to the anatase polymorph of TiO$_2$. In the case of T-10Ni small diffraction peaks at $2\theta = 11.0$, 15.0, 16.2 and 18.6 related to NiTiO$_3$ are also analyzed. These peaks disappeared either when the wt% of Ni increases or Cr was incorporated in the TiO$_2$ network. Moreover, in the sample codoped with the highest content of metallic cations (5%Ni5%Cr) a small peak corresponding to NiO was found.

The TiO$_2$ powders, solely doped with Ni at 10 wt% and calcined at 500°C, revealed a composition comprising a mix anatase-TiO$_2$ and nickel titanate (NiTiO$_3$). The emergence of nickel titanate at 500°C aligns with thermodynamic principles, as the change in Gibbs free energy (ΔG) for the reaction NiO + TiO$_2$ = NiTiO$_3$ reaction is - 4.11 kcal at ambient temperature [14]. Therefore, we can infer that amorphous nickel titanate particles are produced when the nickel precursor (nickel nitrate) is introduced to the titania sol. The transition from the amorphous phase to the crystalline phase in nickel titanate takes place at approximately 500°C.
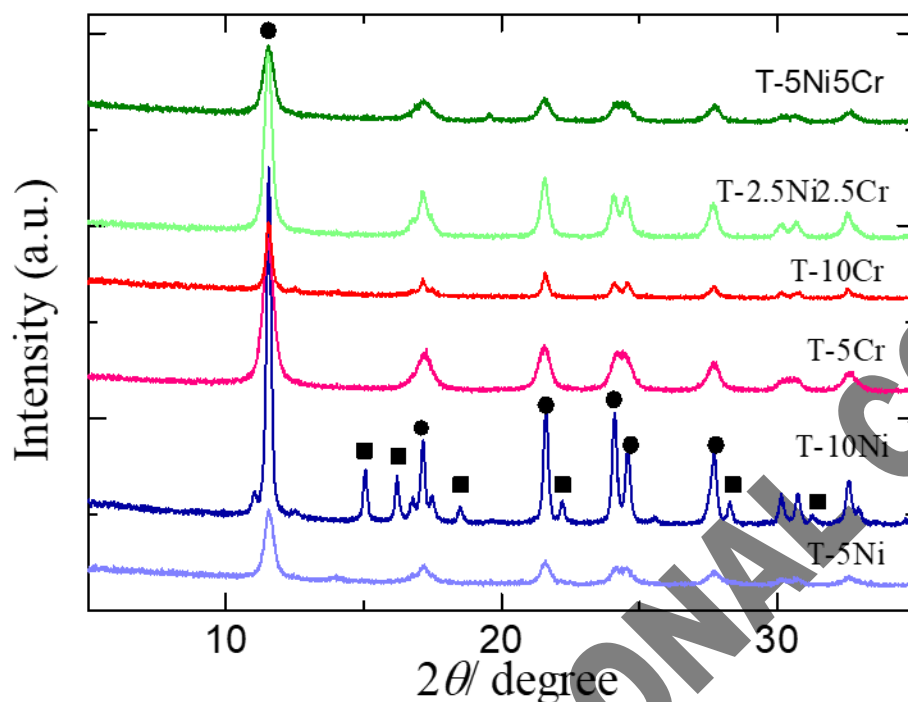
Figure 3. XRD patterns of single and co-doped titania powders annealed at 500°C for 2 h.

($\bullet$ - anatase TiO_2, $\blacksquare$ - $NiTiO_3$)

The X-ray diffraction patterns between 2Theta = 5-40° of the pure TiO_2 show comparable diffraction peaks to those observed in both Ni and Cr single doped and co-doped TiO_2. The Minor peaks corresponding to NiTiO3 and NiO are evident, yet no discernible Ni and Cr phases are observed. This implies the likely incorporation of Ni and Cr ions into the anatase crystal lattice, replacing Ti lattice positions.. Table 1 presents the computed values for 2Theta, d-spacing, crystallite size, and anatase lattice parameters for each of the single-doped and co-doped TiO_2 samples. The data reveals that the doped and co-doped samples exhibit a slight shift towards higher diffraction angles compared to pure TiO_2, indicating a lattice modification in the anatase arrangement due to the incorporation of dopants with reduced ionic radii in the TiO_2 matrix. In metal ion co-doped TiO_2 powder samples, the alteration in the "c" factor is reduced compared to metal ion doped powder samples. This could be due

11

to the different collaboration of dopant ions (Ni and Cr), with the titanium ions in the co-doped TiO_2. Similar observations are reported for all the doped and co-doped TiO_2 samples.

The average particle size and lattice strain of the nanoparticles were estimated from the Rietveld structural analysis for different crystallite sizes using XRD data. X-ray diffraction analysis shows that doped and codoped TiO_2 crystallizes in the tetragonal structure of the anatase phase [34]. In the Rietveld refinement procedure, we employed the Pseudo-Voigt profile function to model the XRD peak profiles and a polynomial function was utilized to model the background. Crystallite size, lattice strain, lattice parameters, and some relevant Rietveld refinement parameters based on the anatase lattice planes of (011) are given in Table 2. It shows that the crystallite size decreases with increasing Ni and Cr content. Examination of the single-doped and co-doped TiO2 samples revealed an average crystallite size ranging from 10.38 to 21.69-nm. The decrease in the crystallite size is probably the result of a deformation process caused by the replacement of Ti ion by the Ni and Cr ions in the anatase structure, since the ionic radius of Ni^{2+} (69 pm) and Cr^{3+} (61.5 pm) are greater than that of Ti^{4+} (60.5 pm). The dopant ions migrate into the TiO_2 crystal lattice and affect the bond lengths in Ti-O-Ti and O-Ti-O, which reduces the crystal growth [35].

Table 2. Structural parameters, strain factor and some relevant parameters for the doped and codoped TiO_2 obtained after Rietveld structure refinement using XRD data.

Sample	Crystallite size (nm)	Lattice strain, ε (%)	Goodness of fit	Anatase lattice parameters (Å)		Volume ($Å^3$)
				a=b	c	
5Ni	12.03	1.01	1.37	3.7913	9.5077	136.66
10Ni	10.38	1.00	1.27	3.8005	9.5154	137.44
5Cr	21.69	0.44	1.12	3.7867	9.5092	136.35
10Cr	16.99	1.63	1.35	3.7931	9.4879	136.51
2.5Ni2.5Cr	19.61	0.88	1.18	3.7907	9.5117	136.68
5Ni5Cr	15.22	1.40	1.14	3.7915	9.4904	136.43

In order to reinforce the findings, the Raman spectra of the obtained samples were examined (Figure 4). This is a technique that is highly sensitive to the arrangement of ions at a local level. It is currently acknowledged that the method of preparation, the existence of impurities, and oxygen deficiencies all have an impact on both the locations and widths of the anatase bands. The Raman active modes of the anatase structure (space group $I4_1/amd$) are located at approximately 158 cm^{-1} (E_g), 197 cm^{-1} (E_g), 399 cm^{-1} (B_{1g}), 519 cm^{-1} (A_{1g}, B_{1g}) and 639 cm^{-1} (E_g) [33].
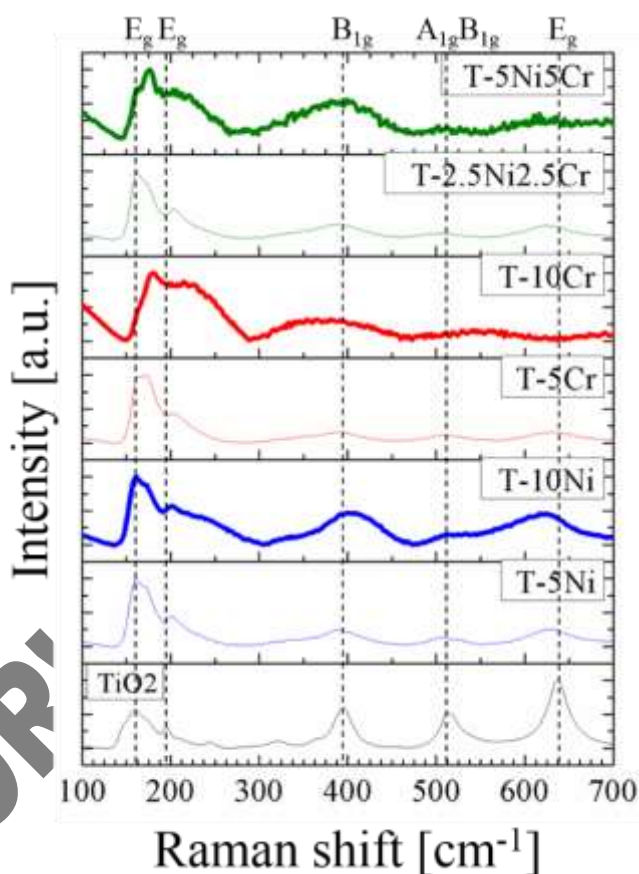
Figure 4. Raman spectra of single and co-doped titania.

Table 3. Assignments and Raman shifts (cm^{-1}) for single and co-doped titania

Assignment	Raman shift (cm^{-1})

|	TiO2	T5Ni	T10Ni	T5Cr	T10Cr	T2.5Ni2.5Cr	T5Ni5Cr
Eg	158	161	161	168	178	163	177
Eg	196	203	203	203	228	203	228
B1g	395	403	395	395	395	395	395
A1g B1g	513	517	509	509	551	509	528
Eg	639	620	630	-	684	-	696

- Means that the band broad until disappeared.

The Raman spectra reveal that the active modes' relative intensity decreases, and the peaks become broader as the amount of Cr and Ni in the NCs increases. In addition, we can see from Table 3 that the EG and A1g+B1g modes are red-shifted in the Cr and Ni co-doped samples. We can rule out that the preparation method is affecting the analyzed results since the co-doped TiO2 samples were prepared using the same procedure as the undoped TiO2 NCs. The position of the dopant ions within the TiO_2 lattice is determined by the discrepancy between the radius of the host ion (i.e., titanium) and the dopant ion's radius [34-35]. The ionic radius of Cr^{3+}, Ni^{2+} and Ti^{4+} are 0.615, 0.690 and 0.605 Å, respectively. Since the difference of the ion radius between Ti^{4+} and the Cr^{3+} and Ni^{2+} is slightly higher, the insertion of the Ni^{2+} and Cr^{3+} is achieved either by replacing Ti^{4+} (substitution) or via interstitial positions. When the Ti^{4+} ions are substituted by Cr^{3+} and Ni^{2+} ions the difference in the ionic radii between the Ti^{4+} and Cr^{3+} and Ni^{2+} results in a lattice deformation of anatase and the resulting strain energy leads to the shift of some of the XRD reflections. Besides that, the peak broadening in the Ni and Cr (co)doped TiO_2 samples is related to oxygen vacancies originated to maintain the charge neutrality when Ti^{4+} ions are replaced by Ni^{2+} and Cr^{3+} ions within the anatase lattice.

The optical band gap energy of the Ni and Cr (co)doped TiO_2 samples were calculated from UV-Vis absorbance data (Figure 5). The absorption coefficient (α) of these samples are calculated by using the Beer-Lambert law. The following Tauc relation was used to calculate the band gap energy [36]:

$$(\alpha h v) = A(h v - E_g)^n, \tag{1}$$

where $h v$ is the incident photon energy, A represents the energy independent constant, E_g stands for the bandgap energy, and the exponent n denotes the nature of the electronic transition. Specifically,

14

in the context of electronic transitions, the exponent 'n' takes on the following values: for indirect allowed transitions $n = 2$, for direct allowed transitions $n = 1/2$, for indirect forbidden transitions $n = 1/3$ and for direct forbidden transitions $n = 2/3$. Usually, allowed transitions ($n = 1/2$ and $n = 2$) dominate the basic absorption processes. The impact of transition metals and the concentration of dopant on the band structure/gap energy was evaluated using eq. (1). The band gap energy was calculated from the intersection points of the tangents to the $(\alpha h\nu)^{1/n}$ curves and the photon energy along the $h\nu$ axis, as shown in Figure 5.
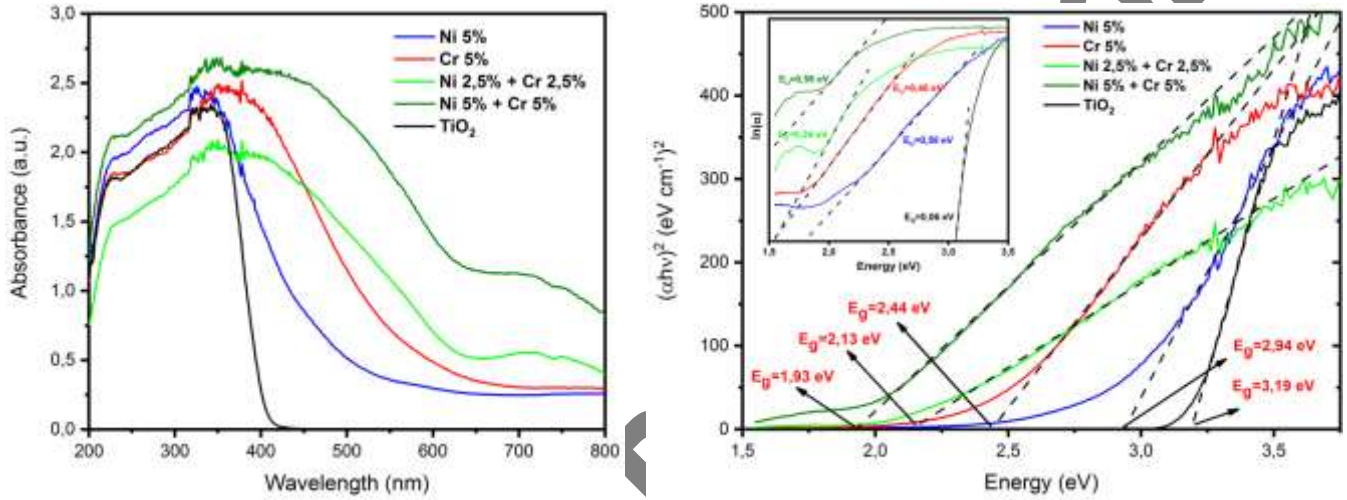
Figure 5. (a) UV-Vis absorption spectra, (b) Tauc and Urbach plots (inset) of TiO_2 NPs.

In a typical optical absorption process, an electron is elevated from the top of the valence band into the base of the conduction band, traversing the band gap. During this shift, some disorder occurs due to the presence of localized tail states originating from the structure of doped and codoped TiO_2. As a result change occurs in the density of the electronic states in the tails of the valence and conduction bands into the energy gap, also referred as the Urbach tail. The Urbach energy, denoting the energy associated with these localized tail states, can be quantified using the subsequent equation (2):

$$\alpha = \alpha_0 \exp\left(\frac{h\nu - E_g}{E_U}\right), \tag{2}$$

where, α_0 stands for a constant value, $h\nu$ represents the incident photon energy, E_g the band-gap energy and E_U the Urbach energy [37]. The Urbach energy was determined by the inverse of the slope of the $h\nu$ and $\ln(\alpha)$ plot in the absorption edge region as shown in Figure 5.

The calculated band gap energy and Urbach energy values are given in Table 3. The findings indicate that the band gap decreases from 3.19 down to 1.93 eV, in response to increasing content of a

15

dopant. Our observations further revealed a rising trend in the Urbach energy in correspondence with the increasing concentration of metal dopants.

The UV-Vis absorbance curves of the synthesized samples are shown in Figure 5a. It was shown that the undoped TiO_2 NCs (black thin line) exhibit strong photoabsorption only at wavelengths lower than 400 nm while the doped samples extend the absorption into the UV-Vis range. The red shift in the reflectance spectra of the (co)doped TiO_2 samples is caused by the inclusion of Ni and Cr within the network of the TiO_2 nanoparticles. The samples doped with Cr have a higher increase in the amplitude of the red shift than those doped with Ni. Moreover, the light absorption increases more with an increase in wt.% of Cr compared to Ni in the TiO_2 structure.

This shift is also noticeable by a change in the color of the NCs from white in the undoped TiO_2 samples to light green in the Cr-doped TiO_2 NCs and dark green in the Ni-doped TiO_2 NCs. The observed shift in color suggests a reduction in the band gap, as shown in the Tauc's plot [37] (Figure 5b) from 3.19 eV for the undoped TiO_2 sample to 2.94, 2.44, 2.13, 1.93 eV for $T5Ni_{500}$, $T5Cr_{500}$, $T2.5Ni2.5Cr_{500}$ and $T5Ni5Cr_{500}$ NCs, respectively.

Table 3. The values for the energy band gap and Urbach energy for both single-doped and co-doped TiO_2 samples.

Sample	Band gap energy (eV)	Urbach energy (eV)
T_{500}	3.19	0.06
$T5Ni_{500}$	2.94	0.58
$T5Cr_{500}$	2.44	0.48
$T2.5Ni2.5Cr_{500}$	2.13	0.36
$T5Ni5Cr_{500}$	1.93	0.56

The absorption spectra of all the samples exhibit the presence of a singular absorption peak, falling within the wavelength range of 400-550 nm. This peak can be attributed to the electronic transition that occurs from the 2p orbital of oxygen to the 3d orbital of titanium. Beyond the aforementioned peak, the (co)doped samples display a range of broad peaks that fall between the wavelengths of 400 and 800 nm. The Cr (co)doped TiO_2 NCs shows two peaks: the initial peak can be seen within the spectral

16

range of 400 to 600 nm is due to the $^4A_2$ (F) to $^4T_1$ (F) transition while the one at around 720 nm is due to the spin forbidden $^4A_2$ (F) to ^2E, $^2T_1$ transition. In the octahedral crystal field, chromium ions in the +3 oxidation state can exhibit these sorts of d–d electronic transitions In the TiO_2 NCs doped with a high content of Ni ($T10Ni_{500}$ and $T5Ni5Cr_{500}$) only a peak at $ca.$ 750 nm was detected within the visible range. This peak is due to the transition from the O2porbital to the Ni3d hybridized orbitals.
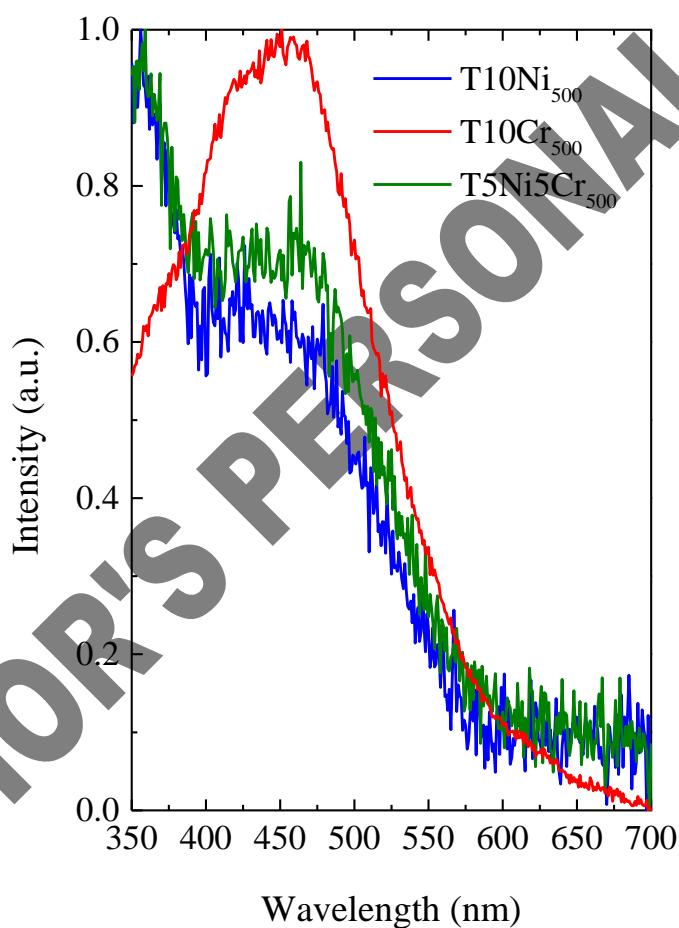
Figure 6. RT steady state fluorescence spectra (λ_{exc}= 325 nm) of $T10Ni_{500}$ (blue line), $T10Cr_{500}$ (red line) and $T5Ni5Cr_{500}$ (green line).

Photoluminescence (PL) emission arises due to electron-hole recombination and the characteristic spectra for our samples are shown in Figure 6. The room temperature PL spectra were recorded for T10Ni$_{500}$, T10Cr$_{500}$ and T5Ni5Cr$_{500}$ NCs with an excitation wavelength of 325 nm. The broad band emission in the 400-550 nm range dominates the PL spectrum of (co)doped TiO$_2$. This shift indicates the relaxation of excited electrons from the 3d level of titanium to the 2p level of oxygen. However, the incorporation of Ni into TiO$_2$ nanoparticles decreases the PL intensity of that transition significantly. The strength of the PL peaks reveals how fast electrons and holes recombine, high strength suggests faster recombination and low strength indicates slower recombination. In the illustration provided, the use of Ni–TiO$_2$ nanoparticles leads to a reduction in intensity, which suggests excellent photoactivity for Ni-(co)doped TiO$_2$ NCs compared to Cr doped TiO$_2$ NCs.

3.2 DFT Calculation results

The band structure of the Ti30Ni6O72 are shown in Figure 7. Accordingly, the lower LUMO conduction band lies at an intermediate point between Γ and Z symmetry, and the highest point of the HOMO valence band is in the X direction. All peak positions are at different points, which means that the material has an indirect bandgap. The direct and indirect bandgap widths are 3.41 and 2.96 eV, respectively, obtained by the GGA-U method for different conduction and valence band positions for Ti30Ni6O72. Figure 7 demonstrates that the lower parts of the conduction band are very differently oriented and oscillate from Γ to A direction. Two impurity levels appear in the middle of the forbidden band and formed by the hybrid 3d Ni electrons and the 2p orbitals of oxygen. The LUMO with energy of 2.98 eV is in point Γ. Due to impurity levels the width of direct bandgap in point Γ slightly widened to value of Eg=3.41 eV comparing Eg=3.3 eV of pure TiO2 (Figure S2 in supporting info). Electron transition from the valence band to the impurity level, which explains the enhansed optical activity of the system (Fig.6).
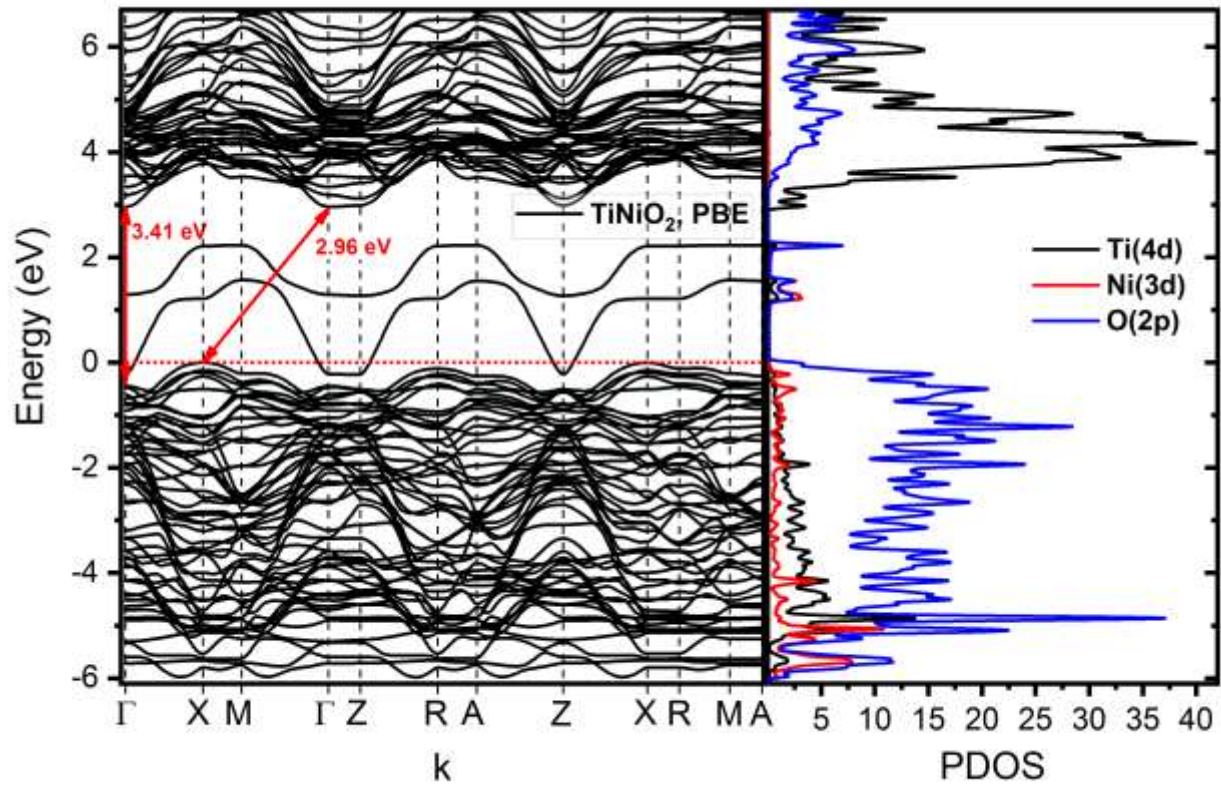
Figure.7. DOS and band structure of Ni doped TiO2 with indirect band gap width of 2.96 eV at X and Γ. Two deep impurity levels are formed in the vicinity of band gap from hybrid of 3d and 2p electronic states of nickel and oxygen atom.
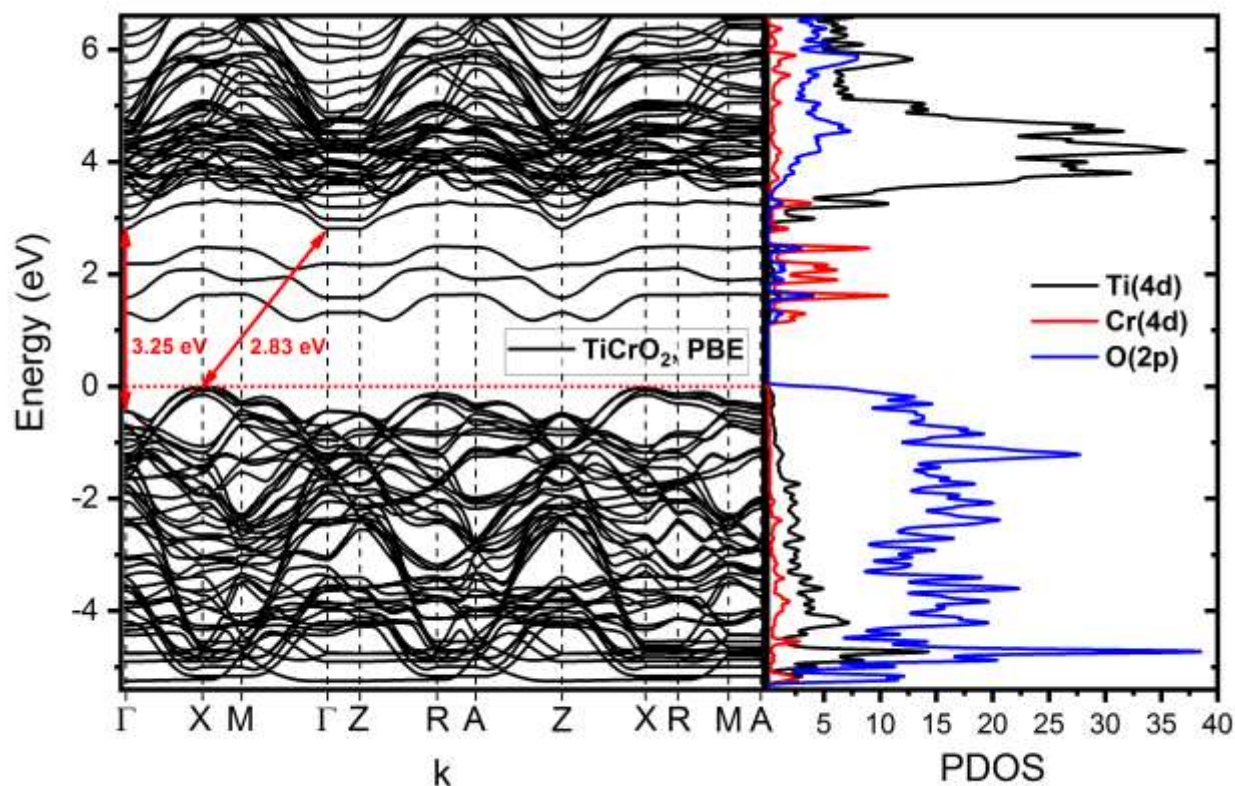
Figure 8. The band structure and PDOS of Cr doped TiO_2, with indirect band gap width of 2.83 eV at X and Γ.

Figure 8 shows the band structure of $Ti_{30}Cr_6O_{72}$. A new band appears in the lower conduction band and the width of the indirect bandgap in X-Γ narrows. It can be seen that 4 impurity levels appear in the middle of the band gap. The lowest level of the conduction band with energy 2.83 eV is at point Γ. Doping TiO2 by chromium atoms does not change the width of the direct band gap and remains like as undoped case E=3.25 eV. New bands appear due to the dzx, dzy, dxy, and d(x2-y2) orbitals of the chromium and the 2p orbitals of oxygen. The electronic orbitals dzx, dzy, dxy, and d(x2-y2) of the chromium atom are half filled and dxz is fully occupied (Fig. S3 in supporting information).
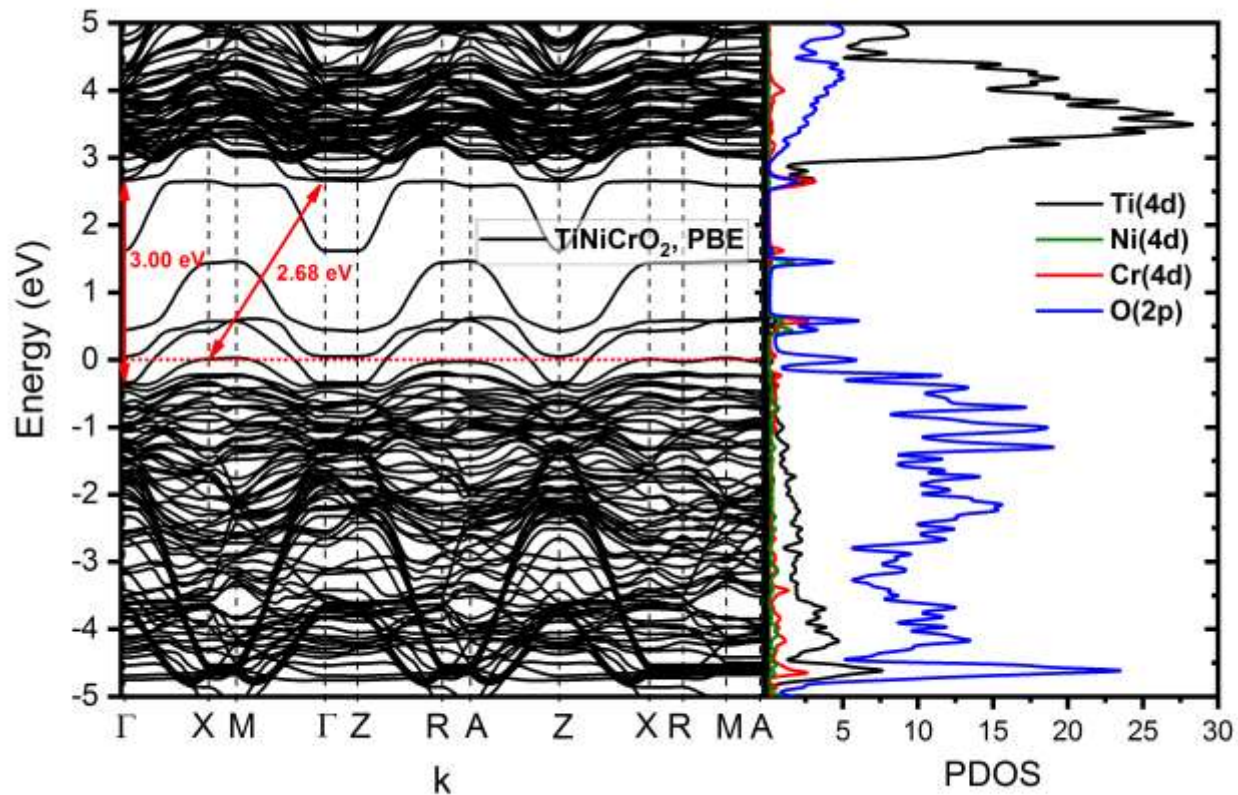
Figure 9. The band structure and DOS of Ni/Cr doped TiO2, with indirect bandgap width of 2.7 eV at points X and Γ. The valence band of TiNiCrO2 consists of a hybrid of 2p-4d orbitals of O and Cr atom, while the conduction band is formed mainly from the 4d orbitals of Ti and Cr.

Co-doping TiO_2 with chromium and nickel atoms narrowed the direct Γ-Γ and indirect X-Γ bandgap widths. Figure 9 shows the electronic structure of $TiNiCrO_2$ with 10 wt.% concentration of nickel and chromium. It can be seen that 4 impurity levels appear in the middle of the bandgap. These energy levels appear due to the 4d orbitals of the Cr and Ni. While valence band maximum lies at X edge, the conduction band minimum located at the point Γ. Due to impurity levels, the width of the direct band gap Γ-Γ is narrowed to E=3.0 eV that explains decreasing of photo-luminescence spectra intensity (Fig.6).

Conclusions

We have established a highly adaptable fabrication method, based on a sol-gel technique to synthesize of TiO_2 nanocrystals. These nanocrystals are doped and co-doped with nickel and chromium metal ions, each exhibiting different ionic radii. The introduction of nickel as a dopant induces a notable shift towards the red end of the spectrum in the light absorption characteristics of TiO_2, considerably reduces its bandgap energy. As a consequence, the altered TiO_2 can capture energy from a larger segment of the visible light spectrum.The results from our characterization studies indicate that TiO_2, when doped with Ni and Cr, stabilizes into an anatase polymorph. This results in a significant reduction in the bandgap energy and modulates the flat band potentials. Consequently, this modified material exhibits promising applicability for photodegradation of waterborne contaminants.It was shown that Cr increases the visible absorption and leads to a lower band gap value compared with the samples doped with Ni. However, Ni (co)doped TiO_2 NCs lead to decrease the PL intensity of the TiO_2 NCs. Systematic studies of the electronic structure of the crystals TiO_2, $(Ti,Cr)O_2$, $(Ti,Ni)O_2$, and $(Ti,Ni,Cr)O_2$ using the density functional theory showed that the band gap width (E_g) of pure TiO_2 reduced when doped with the transition metal ions. In the case of titania doped with Ni(10 wt.%), Cr(10 wt.%) NiCr(5%+5 wt.%), the indirect bandgap values are calculated to be 2.96, 2.83 and 2.7 eV, respectively. Due to the doping with the Ni and Cr ions in the bandgap of the Ni/Cr/TiO_2 system, several impurity levels appear, consisting mainly of the 4d electronic states of Ni and Cr. The levels formed in the band gap region lead to enhancing of photo-sensitivity of Ni/Cr/TiO_2 in the visible light spectrum. In conclusion, the systems studied exhibit photocatalytic properties in the visible and ultraviolet ranges due to the narrowing of the band gap width and significant absorption capacity; however, $TiCrO_2$ may exhibit better photocatalytic properties than $TiNiO_2$. It is expected that this study of the electronic structure and optical properties of $TiCrO_2$, $TiNiO_2$, and $TiNiCrO_2$ will lead to the development of new semiconductor photocatalysts with enhanced activity.

Data Availability Statement

Data will be made available on request.

References

1. Chen, X.; Mao, S. S. Titanium Dioxide Nanomaterials: Synthesis, Properties, Modifications, and Applications. Chem. Rev. 2007, 107, 2891-2959.

2. Spadavecchia, F.; Cappelletti, G.; Ardizzone, S.; Ceotto, M.; Falciola, L. Electronic Structure of Pure and N-Doped Tio2 Nanocrystals by Electrochemical Experiments and First Principles Calculations. J. Phys. Chem. C 2011, 115, 6381-6391.

3. O. Ruzimuradov, S. Nurmanov, M. Hojamberdiev, R.M. Prasad, A. Gurlo, J. Broetz, K. Nakanishi, R. Riedel, Fabrication of nitrogen-doped TiO2 monolith with well-defined macroporous and bicrystalline framework and its photocatalytic performance under visible light, J. Eur. Ceram. Soc. 34 (2014) 809–816.

4. X. Jiang, Y. Zhang, J. Jiang, Y. Rong, Y. Wang, Y. Wu, C. Pan. Characterization of oxygen vacancy associates within hydrogenated TiO2: A positron annihilation study. J. Phys. Chem. C, 2012, 116, 22619-22624.

5. A. Naldoni, M. Allieta, S. Santangelo, M. Marelli, F. Fabbri, S. Cappelli, C. L. Bianchi, R. Psaro, V. D. Santo. Effect of nature and location of defects on bandgap narrowing in black TiO2 nanoparticles. J. Am. Chem. Soc., 2012, 134, 7600-7603.

6. K. Song, X. Han, G. Shao. Electronic properties of rutile TiO2 doped with 4d transition metals: First principles study. J. Alloy Compd., 2013, 551, 118-124.

7. H. Lin, L. Li, M. Zhao, X. Huang, X. Chen, G. Li, R. Yu. Synthesis of high- quality brookite TiO2 single- crystalline nanosheets with specific facets exposed: Tuning catalysts from inert to highly reactive. J. Am. Chem. Soc., 2012, 134, 8328-8331.

8. M. Zhao, H. Xu, H. Chen, S. Ouyang, N. Umezawa, D. Wang, J. Ye. Photocatalytic reactivity of {121} and {211} facets of brookite TiO2 crystals. J. Mater. Chem. A, 2015, 3, 2331-2337.

9. O. Ruzimuradov, G. Hasegawa, K. Kanamori, K. Nakanishi. Preparation of Hierarchically Porous Nanocrystalline CaTiO3, SrTiO3 and BaTiO3 Perovskite Monoliths. J. Amer. Ceram. Soc. 2011. 94. 3335-3339.

10. O. Ruzimuradov, G. Hasegawa, K. Kanamori, K. Nakanishi. Facile Preparation of Monolithic Magnesium Titanates with Hierarchical Porosity. J. Ceram. Soc. Jpn. 2011. 119. 440-444.

11. S. M. Chang, W. S. Liu. The roles of surface- doped metal ions (V, Mn, Fe, Cu, Ce, and W) in the interfacial behavior of TiO2 photocatalysts. Appl. Catal. B Environ., 2014, 156-157, 466-475.

12. S. Sajjad, S. A. K. Leghari, J. Zhang. Copper impregnated ionic liquid assisted mesoporous titania: Visible light photocatalyst. RSC Adv., 2013, 3, 12678-12687.

13. H. Khan, I. K. Swati. Fe3+-doped Anatase TiO2 with d−d Transition, Oxygen Vacancies and Ti3+ Centers: Synthesis, Characterization, UV−vis Photocatalytic and Mechanistic Studies. Ind. Eng. Chem. Res. 2016, 55, 6619−6633.

14. J. Choi, H. Park, M.R.Hoffmann. Combinatorial doping of TiO2 with Pt, Cr, V, and Ni to achieve enhanced photocatalytic activity with visible light irradiation. J. Mater. Res., 2010. 25 (1). 149-158.

15. C. Li, Z. Jiang, Z. Yao. Fabrication and characterization of multi-metal co-doped titania films for a water-splitting reaction. Dalton Trans., 2010, 39, 10692-10696.

16. Guo, J.; Gan, Z.; Lu, Z.; Liu, J.; Xi, J.; Wan, Y.; Le, L.; Liu, H.; Shi, J.; Xiong, R. Improvement of the photocatalytic properties of TiO2 by (Fe+Mo) co-doping - A possible way to retard the recombination process. J. Appl. Phys. 2013, 114, 104903.

17.   Y. Lin, C.Zhu, R.Zhang, X. Hu, X. Zhang, H. Zhu, S.H. Lin. The electronic structure, optical absorption and photocatalytic water splitting of (Fe + Ni) - codoped TiO2: A DFT + U study, International Journal of Hydrogen Energy. 2017, 42 (8), 4966-4976.

18.   A. Garg, A. Singh, V.K. Sangal, P.K. Bajpai, N. Garg, Synthesis, Characterization and anticancer activities of metal ions Fe and Cu doped and co-doped TiO2 New J. Chem., 2017, 41, 9931-9937.

19.   Márquez, A. M.; Plata, J. J.; Ortega, Y.; Sanz, J. F.; Colón, G.; Kubacka, A.; Fernández-García, M. Making Photo-Selective Tio2 Materials by Cation–Anion Codoping: From Structure and Electronic Properties to Photoactivity. J. Phys. Chem. C 2012, 116, 18759-18767.

20.   Breault, T. M.; Bartlett, B. M. Composition Dependence of Tio2:(Nb,N)-X compounds on the Rate of Photocatalytic Methylene Blue Dye Degradation. J. Phys. Chem. C 2013, 117, 8611-8618.

21.   O. Ruzimuradov, K. Sharipov, A. Yarbekov, K. Saidov, M. Hojamberdiev, R.M. Prasad, G. Cherkashinin, R. Riedel, A facile preparation of dual-phase nitrogen-doped TiO2-SrTiO3 macroporous monolithic photocatalyst for organic dye photodegradation under visible light, J. Eur. Ceram. Soc. 2015, 35, 1815-1821.

22.   O. Ruzimuradov, M. Hojamberdiev, C. Fasel, R. Riedel. Fabrication of lanthanum and nitrogen – co-doped SrTiO3 – TiO2 heterostructured macroporous monolithic materials for photocatalytic degradation of organic dyes under visible light. J. Alloys Comp. 699 (2017) 144–150.

23.   R. K. Eraiah, G. Madras. Metal–metal charge transfer and interfacial charge transfer mechanism for the visible light photocatalytic activity of cerium and nitrogen co-doped TiO2. J Sol-Gel Sci Technol (2014) 71:193–203.

24.   C. Marchiori, G.Di Liberto, G. Soliveri, L. Loconte, L.Lo Presti, D. Meroni, M. Ceotto, C. Oliva, S. Cappelli, G. Cappelletti, C. Aieta, S. Ardizzone. Unraveling the Cooperative Mechanism of

Visible light Absorption in Bulk N,Nb - Codoped TiO2 nanopowders. J. Phys. Chem. C, 2014, 118 (41), 24152–24164.

25.   M. Numata, R. Takahashi, I. Yamada, K. Nakanishi, S. Sato. Sol–gel preparation of Ni/TiO2 catalysts with bimodal pore structures. Appl. Catal. A: Gen. 2010, 383, 66-72.

26.   Tong Zhu and Shang-Peng Gao, The Stability, Electronic Structure, and Optical Property of TiO$_2$ Polymorphs, J. Phys. Chem. C 2014, 118, 11385−11396.

27. P. Giannozzi, O. Andreussi, T. Brumme, O. Bunau, M. Buongiorno Nardelli, M. Calandra, R. Car, C. Cavazzoni, D. Ceresoli, M. Cococcioni, N. Colonna, I. Carnimeo, A. Dal Corso, S. de Gironcoli, P. Delugas, A. R. DiStasio, Jr., A. Ferretti, A. Floris, G. Fratesi, G. Fugallo, R. Gebauer, U. Gerstmann, F. Giustino, T. Gorni, J. Jia, M. Kawamura, H.-K. Ko, A. Kokalj, E. Küçükbenli, M. Lazzeri, M. Marsili, N. Marzari, F. Mauri, N. L. Nguyen, H.-V. Nguyen, A. Otero-de-la Roza, L. Paulatto, S. Poncé, D. Rocca, R. Sabatini, B. Santra, M. Schlipf, A. Seitsonen, A. Smogunov, I. Timrov, T. Thonhauser, P. Umari, N. Vast, X. Wu, and S. Baroni, Advanced capabilities for materials modelling with Quantum ESPRESSO, J. Phys.: Condens. Matter 29, 465901 (2017).

28. Nguyen, Trang, Tran, Nam, Bach Thanh Cong. Influences of metallic doping on anatase crystalline titanium dioxide: From electronic structure aspects to efficiency of TiO$_2$-based dye sensitized solar cell (DSSC) // Material Chem. Phys. 2014. V. 144, pp. 114-121.

29. Hou X.G., Liu A.D., Huang M.D., Liao B., Wu X.L.: First-principles band calculations on electronic structures of Ag-doped rutile and anatase TiO$_2$. Chin. Phys. Lett. 2009, 26:077106.

30. Himmetoglu B., Floris A., De Gironcoli S., Cococcioni M. Hubbard-corrected DFT energy functionals: The LDA+U description of correlated systems. International Journal of Quantum Chemistry. 2014, 114:14-49.

31. Ansam Hadi Hasan and Falah H. Ali, Synthesis of Cr Doped TiO2 Using Sol-Gel Technique and Calculation of its Photocatalytic Activity, Indian Journal of Natural Sciences, 2018, 9(51), 15242-15249.

32. M. Shaban, A.M. Ahmed, N. Shehata, M.A. Betiha, A.M. Rabie, Ni-doped and Ni/Cr co-doped TiO_2 nanotubes for enhancement of photocatalytic degradation of methylene blue. Journal of Colloid and Interface Science 2019, 555, 31-41.

33. Saturnino Marco Lupi, Pietro Galinetto, Benedetta Albini, Elisa Di Ronza, Silvana Rizzo and Ruggero Rodriguez y Baena. Micro-Raman Spectroscopy of Dental Implants Subjected to Different Surface Treatments, Appl. Sci. 2020, 10, 2417.

34. Rietveld HM. A profile refinement method for nuclear and magnetic structures. J Appl Cryst. 1969, 2:65-71.

35. Manzoor M, Rafq A, Ikram M, Nafees M, Ali S 2018 Int. Nano Lett. 8 1−8

36. Tauc J, in: F Abeles (Ed.), Optical properties of solids (North-Holland, Amsterdam, 1972)

37. Urbach, Franz. "The Long-Wavelength Edge of Photographic Sensitivity and of the Electronic Absorption of Solids". Physical Review. (1953) 92(5): 1324